

**ES021**

**Adjoint Optimisation of Multi-Angle  
Achromatic Metalenses**

## 1 INTRODUCTION

Contemporary studies in ultra-thin metasurface structures have garnered widespread traction, largely due to its versatility in expanding upon diffractive optics and its potential in imaging and focusing applications. These patterned optical thin films (shown in Fig. 1) provide unprecedented precision compared to bulky conventional-optics collimating lenses, especially in fields like biomedical imaging<sup>[1]</sup>, spectroscopy<sup>[2]</sup>, and augmented reality<sup>[3]</sup>. The diverse capabilities of metasurfaces have cemented them as an increasingly integral component of photonics, actualising miniaturised, low-cost, and high-performance optical systems.

However, a challenging hindrance presents in the design of such structures. Classical optimisation methods are highly time-consuming, bottlenecking the feasibility of complex manipulation functionalities. Furthermore, standard unit-cell approaches have been shown to perform sub-optimally when it comes to creating broadband metasurface lenses (metalenses) of high numerical apertures<sup>[4]</sup>. To eschew the limitations of traditional methods, inverse design (also known as topological optimisation) has been extensively explored as a means of achieving high-efficiency metalenses, enabling rapid gradient computation with respect to numerous structural degrees of freedom via the adjoint method. This technique has been historically used in fields like circuit theory<sup>[5]</sup> and deep learning<sup>[6,7]</sup>, and has demonstrated state-of-the-art practicality as a tool for furthering the study of nanophotonic metalenses.

This paper explores the design of sub-wavelength metalenses, using inverse design as an algorithmic approach to optimising the desired manipulation of light waves. Subsequently, we exploit Lorentz reciprocity via the adjoint method, offering efficient gradient calculation of electric-field objective functions<sup>[8]</sup>. We apply a mathematical filter for two-dimensional binary metalenses, and implement epigraph formulation for differentiable maximin optimisation. We then generate metalens designs that cover numerical apertures 0.1 to 0.5, as well as a wide incident angle of  $15^\circ$ , providing industry-suitable models and demonstrating far-reaching efficacy of the presented optimisation process.

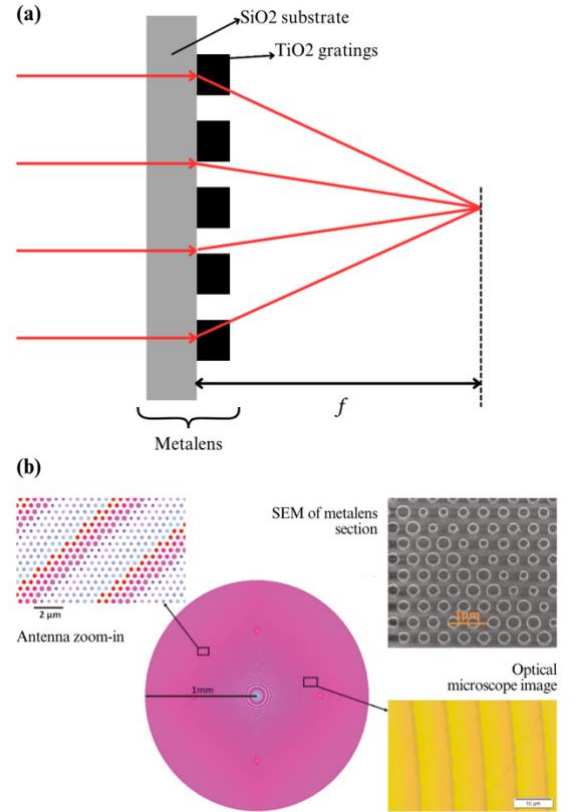


**Figure 1:** (a) 2-dimensional schematic of grating-based metalenses with focal length  $f$ . (b) Microscopic design patterns of circular Huygens metalenses.

## 2 METHODOLOGY

### 2.1 Inverse Design

For a structure with a well-defined geometry, calculating the resultant electromagnetic fields passing through it presents a forward problem that can be resolved by solving Maxwell's equations. Contrariwise, electromagnetic inverse design is concerned with the antagonistic intention of finding the required geometry for a desired functionality<sup>[9]</sup>. Such a problem maximises the objective function  $F$  while being subject to the four Maxwell equations:

$$\begin{cases} \max & f(\mathbf{E}, \mathbf{H}, \omega) \\ \text{s. t.} & \nabla \cdot \epsilon \mathbf{E} = \rho \\ & \nabla \cdot \mu \mathbf{H} = 0 \\ & \nabla \cdot \mathbf{E} = -j\omega\mu\mathbf{H} \\ & \nabla \cdot \mathbf{H} = \mathbf{J} + j\omega\epsilon\mathbf{E} \end{cases}$$

where the goal is to find the permittivity tensor  $\epsilon$  and permeability tensor  $\mu$  that maximises the objective function  $f$ , which is the electric field intensity at the focal point (i.e.  $f = |E_z(\mathbf{r}_0)|^2$ ).

In facilitating inverse design, we introduce the adjoint method, an optimisation technique used for multifactorial designs by introducing an adjoint electromagnetic field  $\mathbf{A}$  auxiliary to the direct field  $\mathbf{E}$ , which is obtained by back-propagating the intended field response backwards through the metastructure. Direct computation via a singular set of dipole sources eliminates the necessity of conducting separate simulations for each geometric modification, leading to dramatically efficient structural updates<sup>[10,11]</sup>. This is schematically illustrated in Fig. 2.

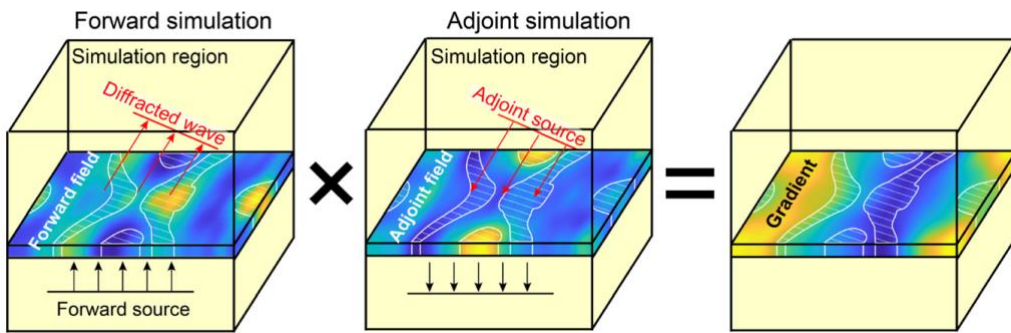


**Figure 2:** Conceptual representation of adjoint method formulation (Park et al, 2022)

Using Lorentz's reciprocity principle for electromagnetism, for a small volume  $dV$  having a permittivity perturbation  $\delta\epsilon_r$ , the gradient of  $f$  is calculated using both direct and adjoint fields.

$$\frac{\delta f}{\delta \epsilon_r} = \text{Re}(\mathbf{A} \cdot \mathbf{E})$$

Since  $f$  is calculated analytically in the direct run, all variables can be obtained and optimised through iterative applications of a gradient descent method, ultimately leading to an optimum. The permittivity function describes the material structure, and maps each point to a value between 0 and 1 corresponding to two materials with respective permittivities  $\epsilon_{r_1}$  and  $\epsilon_{r_2}$ .

## 2.2 Binary Penalisation

In all presented designs,  $\text{TiO}_2$  is chosen as the primary metastructure material, alongside gaps of plain air. Accounting for manufacturability, each point must have a singular, well-defined material, rendering intermediate values from topological optimisation unsuitable. Consequently, we enforce a binary-material constraint by implementing binary penalisation during convergence of the optimal structure. For a design projection, this is achieved by introducing a thresholding parameter  $\beta$  that is steadily increased every few optimisation iterations. The metastructure is then adjusted using the “hat filter” equation below, denoted  $H(x)$ , with the parameter  $\eta$  serving as the mapping threshold, thus allowing the filter to act as a smooth approximation to the intermediate Heaviside step function<sup>[12,13]</sup>.

$$H(x) = \frac{\tanh(\beta\eta) + \tanh(\beta(x - \eta))}{\tanh(\beta\eta) + \tanh(\beta(1 - \eta))}$$

Referencing the previous section, we choose plain air and  $\text{TiO}_2$  to correspond with absolute values 0 and 1 respectively, with their accompanying permittivities.

## 2.3 Optimisation Process

In optimising the metastructure, we begin with filtering and projection. A forward run is executed to evaluate the value of our objective function, followed by an adjoint run initiated from the desired focal point. Gradient calculations are performed using the method of moving asymptotes<sup>[14]</sup>, and this procedure is iterated with increasing binarization.

For forward runs, the electromagnetic finite-difference time-domain (FDTD) method is used to solve Maxwell’s time-dependent curl equations. This method involves dividing space and time into a discrete Yee lattice, and updating the electromagnetic fields at each grid junction based on their neighbouring values, as well as the local sources of those fields<sup>[15,16]</sup>. Berenger’s perfectly matched layers (PMLs) are concurrently implemented to satisfy boundary conditions, where fields are dampened as they propagate into the absorbing medium<sup>[17]</sup>.

For our study of achromatic metalenses, the design can be represented as a maximin optimisation problem over distinct objective functions subject to Maxwell’s equations spanning  $N$  frequency points,

with objective functions  $f_k$ ,  $k \in \{1, 2, \dots, N\}$  unique to each field pattern  $\mathbf{E}$ . The optimisation of the worst-case performance across the visible light spectrum ensures that every frequency correlates to an adequate degree of efficiency.

$$\max F(x) = \min\{f_1(\mathbf{E}), f_2(\mathbf{E}), \dots, f_N(\mathbf{E})\}$$

It is observable that this problem does not guarantee differentiability across all intervals, thus diminishing the efficacy of gradient-based optimisation algorithms. To remedy this, we apply epigraph formulation, introducing a dummy variable  $t$  and recasting the non-differentiable maximin problem into a differentiable maximisation problem with additive nonlinear constraints<sup>[4,12]</sup>.

$$\max t, \text{ s.t. } f_k(\mathbf{E}) - t \geq 0$$

## 2.4 Simulation

For optimisation and design purposes, we use MEEP, an open-source Python FDTD solver equipped with an adjoint solver for inverse design<sup>[18]</sup>. We design achromatic lenses that concurrently optimise the focusing of light of wavelengths between 400nm and 700nm. As seen in Fig. 3, design region of the single-layered metalens (hatched blue) has a width  $12.5\mu\text{m}$ , a thickness  $0.25\mu\text{m}$ , and will be integrated with  $\text{TiO}_2$  material. The lens is mounted on a  $\text{SiO}_2$  slab (black) and focuses the light in plain air (white). A Gaussian light source is placed directly below the lens (red line), emitting  $E_z$ -polarised light at all frequencies. The boundaries of the cell represent PMLs (hatched green), absorbing incoming light with zero reflection. A monitor is placed right above the lens (blue line), measuring the fields and mathematically inferring the focal point intensity using the near-to-far-field transformation implemented in MEEP<sup>[19]</sup>. The average intensity at the focal point per is then maximised using MEEP's built-in adjoint solver. MEEP offers the specification of a minimum feature size that limits the width of a  $\text{TiO}_2$  segment, enabling lithographical feasibility and non-robustness in metastructure manufacturing, which we set across all designs to be 25nm.

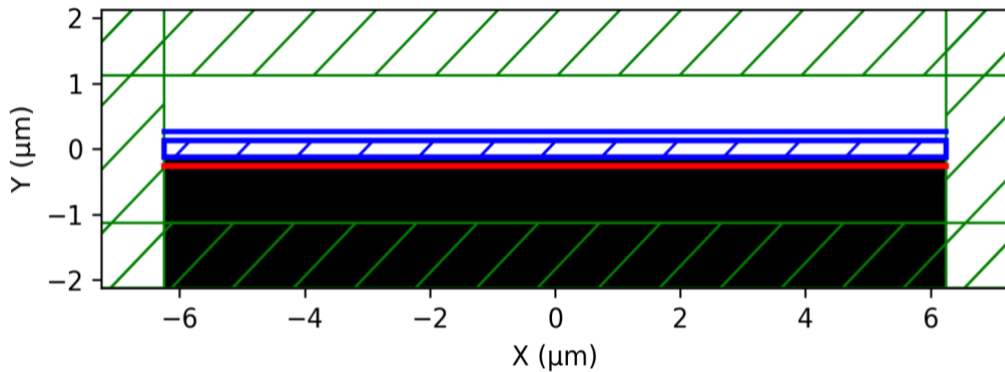


*Figure 3: Metalens design region, as implemented in Meep.*

### 3 RESULTS & DISCUSSION

#### 3.1 Achromatic Metalenses

In this section, we fabricate low and medium-NA achromatic metalenses, thereby presenting structural designs capable of achieving broadband light focusing at distinct focal points. This highlights the adaptability of our optimisation process, demonstrating versatile customisation through parameter adjustment. We optimise metalens structures at 5 numerical apertures from 0.1 to 0.5, and achromatically, with reference to 7 wavelengths, between 400nm and 700nm in regular 50nm intervals. The metalens geometry is implemented with vertical-axis symmetry about  $x = 0$ . The optimised design, normalised intensity, and pseudocolour plots displaying light propagation behaviour per wavelength for the 0.1 NA (focal length  $x_1 = 62.0\mu\text{m}$ ) metalenses are showcased in Fig. 4.

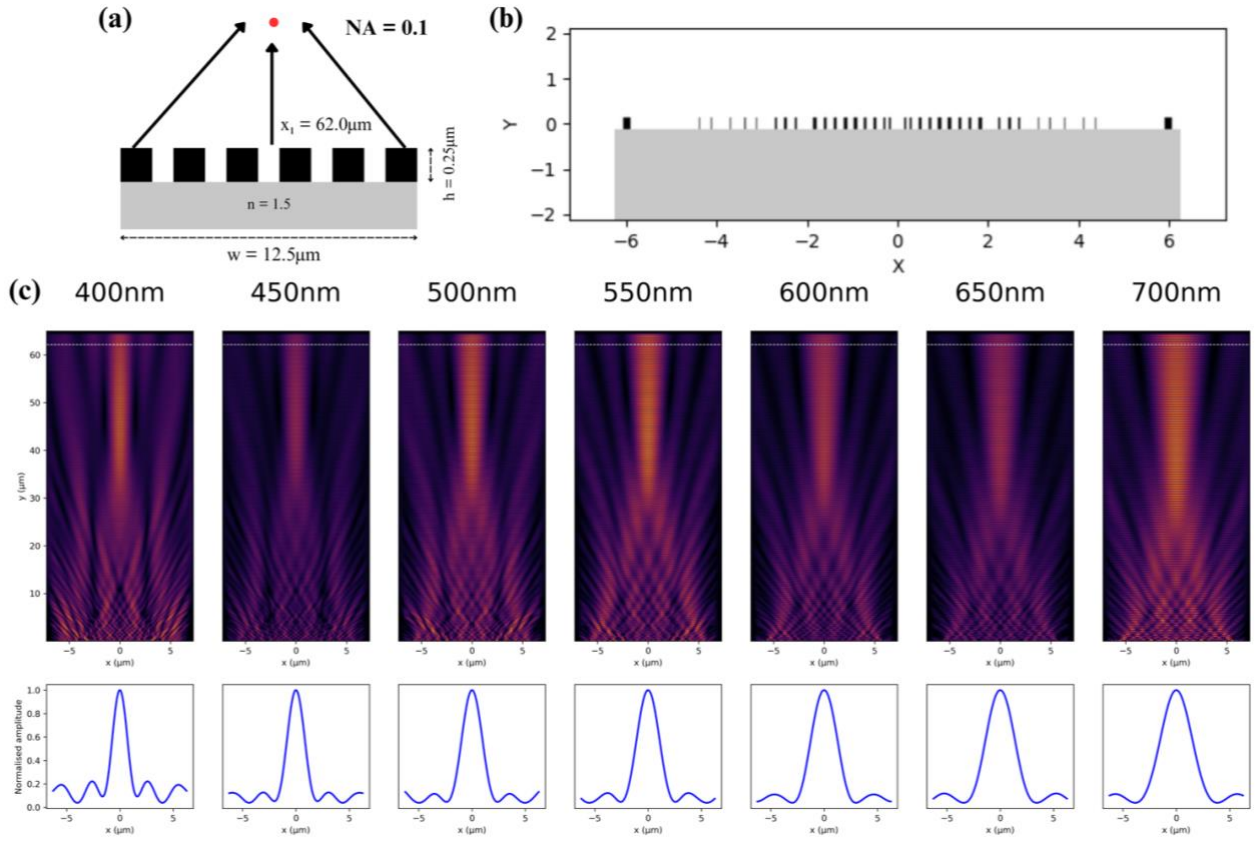


**Figure 4:** 0.1 NA, achromatic metalens for visible-spectrum wavelengths. (a) Metalens and focal dimensions. (b) Optimised metalens design. (c) Field propagation of metalens-focused light with normalised amplitude curves (taken at white line).

For medium-NA design capabilities, Fig. 5 shows similar illustrations for 0.5 NA metalenses. The focal length remains nearly constant across all wavelengths, characteristic of proper achromatic metalenses. It is evident that light is greatly concentrated at the intended focal point, thus indicating high-efficiency focusing across low and medium-NA photonic devices, with minimal stray dispersion.



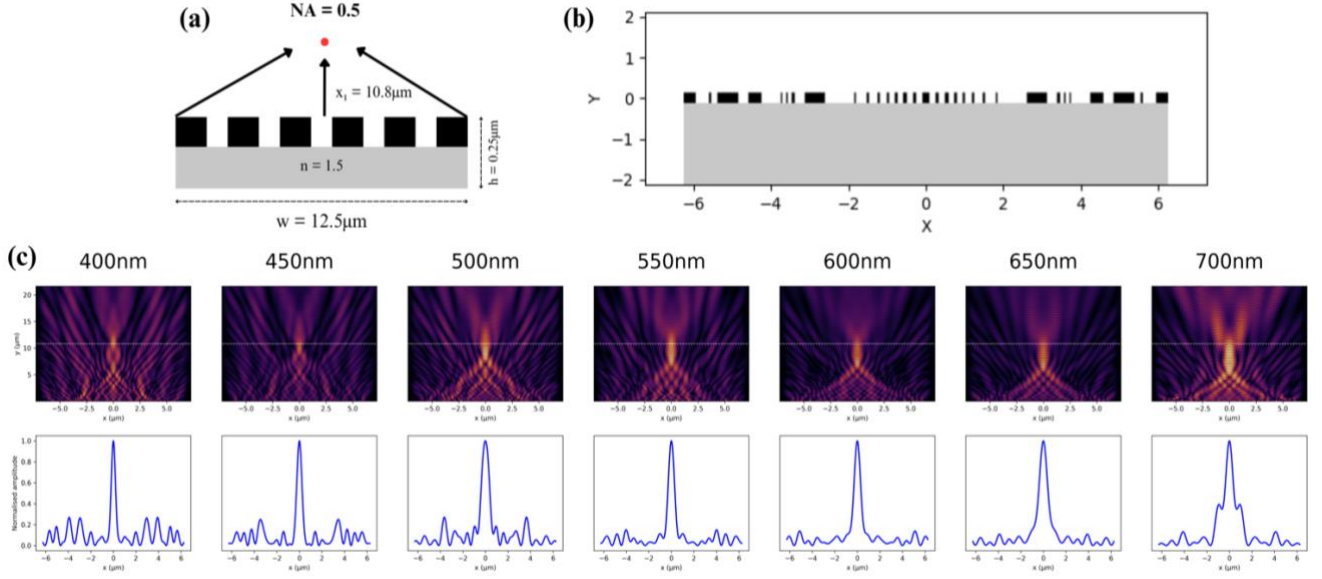


**Figure 5:** 0.5 NA, achromatic metalens for visible-spectrum wavelengths. (a) Metalens and focal dimensions. (b) Optimised metalens design. (c) Field propagation of metalens-focused light with normalised amplitude curves (taken at white line).

### 3.2 Achromatic & Wide Field-of-View (WFOV) Metalenses

This section presents the optimisation of achromatic WFOV metalenses, presenting designs for focusing metalenses adapted to planewaves propagated at oblique incident angles<sup>[20-22]</sup>. This is performed by incorporating a custom wavevector  $\mathbf{k}$  directed at an angle  $\theta$  into the source (calculated

clockwise from the normal of the metalens), and creating a spatially varying amplitude function  $a = e^{i(2\pi\mathbf{k}\cdot(\mathbf{x}+\mathbf{x}_0))}$ , where  $\mathbf{x}$  is the position of evaluation and  $\mathbf{x}_0$  is the wave offset position (the centre of the source). We optimise metalens structures at a numerical aperture of 0.3 ( $x_1 = 19.9 \mu\text{m}$ ), with three wavelengths 500nm, 600nm, and 700nm. In wide-angle metalenses, it is important to note the lateral shift in angular difference, whereby the focal point is horizontally offset across the length of the metalens by  $x_1 \tan(\theta)$ . This is demonstrated in

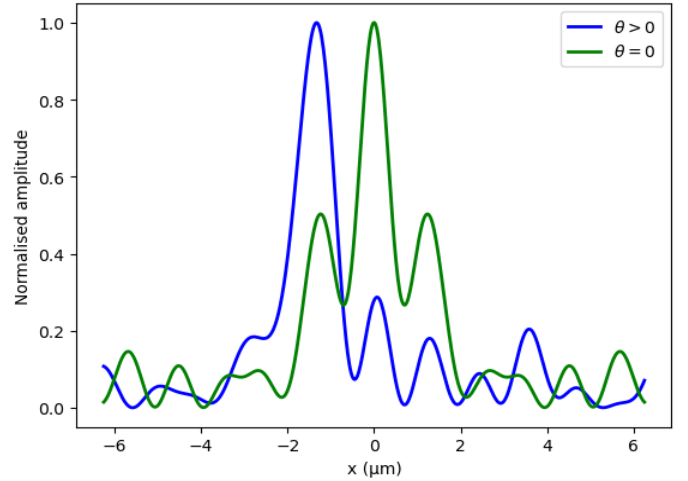


**Figure 6:** Normalised amplitude for zero-angle metalens (green) and positive-angle metalens (blue). The focal point under positive incident angles is shifted leftwards.

Fig. 6, where two metalenses are designed with the exact same parameters, except for a differing  $\theta$ . Below, Fig. 7 displays simulation results for the optimised metalenses for a 15° anticlockwise incident planewaves. We do not enforce any geometrical symmetry for this particular section. As similar to

Section 3.1, we find that distributions along the propagating direction are highly concentrated within the intended focal point, validating its WFOV properties across a sufficient spectral range.

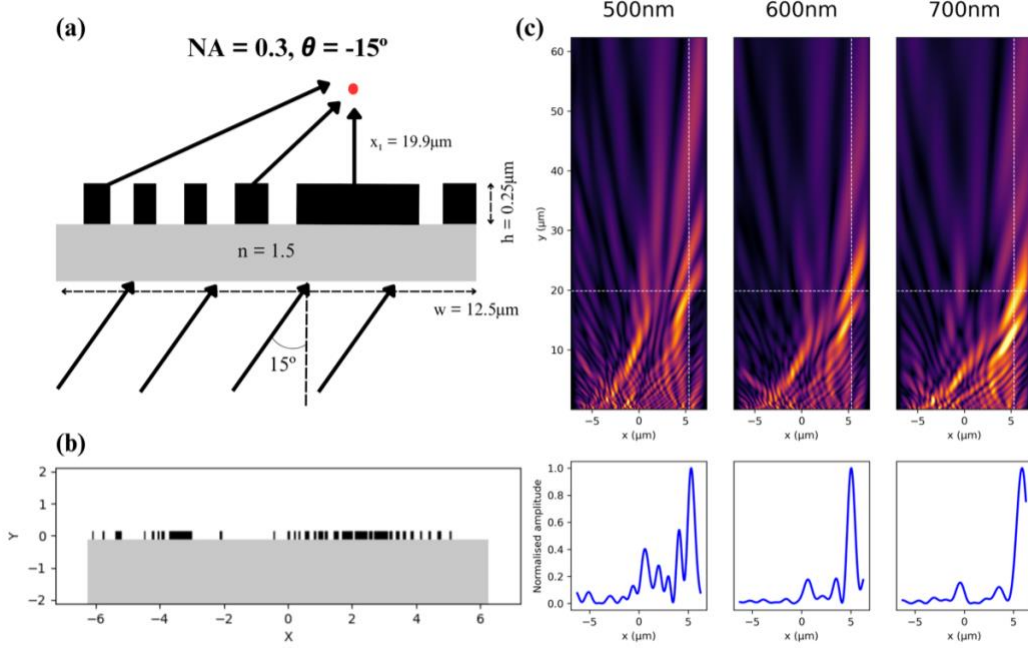


**Figure 7:** 0.3 NA,  $15^\circ$  achromatic wide-angle metalenses optimised for 500–700nm wavelengths. (a) Metalens dimensions. (b) Optimised metalens design. (c) Field propagation of metalens-focused light with normalised amplitude curves (taken at white line).

#### 4 CONCLUSION

To conclude, we successfully demonstrate the adjoint optimisation of single-layered achromatic metalenses that achieves efficient focusing across several numerical apertures. The nano-structural gratings of our metalenses also ensures feasibility in metastructure manufacturability, including complementary metal-oxide-semiconductor (CMOS) fabrication processes. Additionally, our research extends to WFOV designs, integrating oblique incidence capabilities whilst maintaining achromatic properties over a smaller spectral range. In our MEEP simulations, the focal intensity distributions of light are concentrated appropriately, thereby indicating correction of chromatic and angular aberrations. With this, our research achieves a milestone in flat optics by simultaneously realising achromatic functionality with wide fields-of-view, a heavily-sought goal in the field. Whilst results are promising, the focus is still imperfect, which may be due to limitations with current physics and configuration settings. By performing inverse design of multi-layered structures, much better efficiency can be achieved. Our work also underscores the computational viability of the optimisation framework, offering a cost-effective approach to nanophotonic design. We believe that our findings can function positively towards the state-of-the-art, contributing towards widespread efforts in furthering compact dielectric metastructure optics for use in areas like spectroscopy and microscopy.



**BIBLIOGRAPHY**

1. Wang, Y., Chen, Q., Yang, W., Ji, Z., Jin, L., Ma, X., Song, Q., Boltasseva, A., Han, J., Shalae, V. M., & Xiao, S. (2021). High-efficiency broadband achromatic metalens for near-IR biological imaging window. *Nature Communications*, 12(1). <https://doi.org/10.1038/s41467-021-25797-9>
2. Li, Z., Palacios, E., Butun, S., & Aydin, K. (2015). Visible-Frequency metasurfaces for broadband Anomalous Reflection and High-Efficiency Spectrum Splitting. *Nano Letters*, 15(3), 1615–1621. <https://doi.org/10.1021/nl5041572>
3. Li, Y., Chen, S., Liang, H., Ren, X., Luo, L., Ling, Y., Liu, S., Su, Y., & Wu, S. (2022). Ultracompact multifunctional metalens visor for augmented reality displays. *Photonix*, 3(1). <https://doi.org/10.1186/s43074-022-00075-z>
4. Chung, H., & Miller, O. D. (2020). High-NA achromatic metalenses by inverse design. *Optics Express*, 28(5), 6945. <https://doi.org/10.1364/oe.385440>
5. Director, S., & Rohrer, R. (1969). The generalized adjoint network and network sensitivities. *IEEE Transactions on Circuit Theory*, 16(3), 318–323. <https://doi.org/10.1109/tct.1969.1082965>
6. Rumelhart, D. E., Hinton, G. E., & Williams, R. J. (1986). Learning representations by back-propagating errors. *Nature*, 323(6088), 533–536. <https://doi.org/10.1038/323533a0>
7. LeCun, Y., Boser, B., Denker, J. S., Henderson, D., Howard, R. E., Hubbard, W., & Jackel, L. D. (1989). Backpropagation applied to handwritten Zip code recognition. *Neural Computation*, 1(4), 541–551. <https://doi.org/10.1162/neco.1989.1.4.541>
8. Altman, C., & Suchy, K. (1998). The Maxwell and adjoint systems for complex media: Physical significance and applications. *International Journal of Applied Electromagnetics and Mechanics*, 9(2), 135–142. <https://doi.org/10.3233/jaem-1998-111>
9. Miller, O. D. (2013). Photonic design: From fundamental solar cell physics to computational inverse design. *arXiv (Cornell University)*. <https://doi.org/10.48550/arxiv.1308.0212>
10. Molesky, S., Lin, Z., Piggott, A. Y., Jin, W., Vucković, J., & Rodriguez, A. W. (2018). Inverse design in nanophotonics. *Nature Photonics*, 12(11), 659–670. <https://doi.org/10.1038/s41566-018-0246-9>
11. Park, J., Kim, S., Nam, D. W., Chung, H., Park, C. Y., & Jang, M. S. (2022). Free-form optimization of nanophotonic devices: from classical methods to deep learning. *Nanophotonics*, 11(9), 1809–1845. <https://doi.org/10.1515/nanoph-2021-0713>

12. Lazarov, B. S., Wang, F., & Sigmund, O. (2016). Length scale and manufacturability in density-based topology optimization. *Archive of Applied Mechanics*, 86(1–2), 189–218. <https://doi.org/10.1007/s00419-015-1106-4>
13. Hammond, A. M., Oskooi, A., Johnson, S. G., & Ralph, S. E. (2021). Photonic topology optimization with semiconductor-foundry design-rule constraints. *Optics Express*, 29(15), 23916. <https://doi.org/10.1364/oe.431188>
14. Svanberg, K. (1987). The method of moving asymptotes—a new method for structural optimization. *International Journal for Numerical Methods in Engineering*, 24(2), 359–373. <https://doi.org/10.1002/nme.1620240207>
15. Yee, N. K. (1966). Numerical solution of initial boundary value problems involving maxwell's equations in isotropic media. *IEEE Transactions on Antennas and Propagation*, 14(3), 302–307. <https://doi.org/10.1109/tap.1966.1138693>
16. Taflove, A., & Brodwin, M. (1975). Numerical solution of Steady-State electromagnetic scattering problems using the Time-Dependent Maxwell's equations. *IEEE Transactions on Microwave Theory and Techniques*, 23(8), 623–630. <https://doi.org/10.1109/tmtt.1975.1128640>
17. Berenger, J. (1994). A perfectly matched layer for the absorption of electromagnetic waves. *Journal of Computational Physics*, 114(2), 185–200. <https://doi.org/10.1006/jcph.1994.1159>
18. Oskooi, A. F., Roundy, D., Ibanescu, M., Bermel, P., Joannopoulos, J., & Johnson, S. G. (2009). Meep: A flexible free-software package for electromagnetic simulations by the FDTD method. *Computer Physics Communications*, 181(3), 687–702. <https://doi.org/10.1016/j.cpc.2009.11.008>
19. Umashankar, K., & Taflove, A. (1982). A novel method to analyze electromagnetic scattering of complex objects. *IEEE Transactions on Electromagnetic Compatibility, EMC-24*(4), 397–405. <https://doi.org/10.1109/temc.1982.304054>
20. Yang, F., Shalaginov, M. Y., Lin, H., An, S., Agarwal, A., Zhang, H., Rivero-Baleine, C., Gu, T., & Hu, J. (2023). Wide field-of-view metalens: a tutorial. *Advanced Photonics*, 5(03). <https://doi.org/10.1117/1.ap.5.3.033001>
21. Hongli, Y., Zhaofeng, C., & Xiaotong, L. (2022). Achromatic and wide field of view metalens based on the harmonic diffraction and a quadratic phase. *Optics Express*, 30(25), 45413. <https://doi.org/10.1364/oe.475337>
22. Tang, D., Chen, L., Liu, J., & Zhang, X. (2020). Achromatic metasurface doublet with a wide incident angle for light focusing. *Optics Express*, 28(8), 12209. <https://doi.org/10.1364/oe.392197>

## ANNEX

### A. Focusing Efficiency

The focusing efficiency of a metalens is taken to be the percentage of the focusing intensity (the intensity of the electric field along the focal plane) over the input intensity.

For our study in achromatic metalenses, we plot the focusing efficiency across all accounted wavelengths (400nm, 450nm, 500nm, 550nm, 600nm, 650nm, and 700nm). This is done for all simulated numerical apertures from 0.1 to 0.9 and displayed in Fig. A below. We typically observe that focusing efficiency is decreased in lower numerical apertures, likely due to the longer focal length resulting in greater dispersion of light.

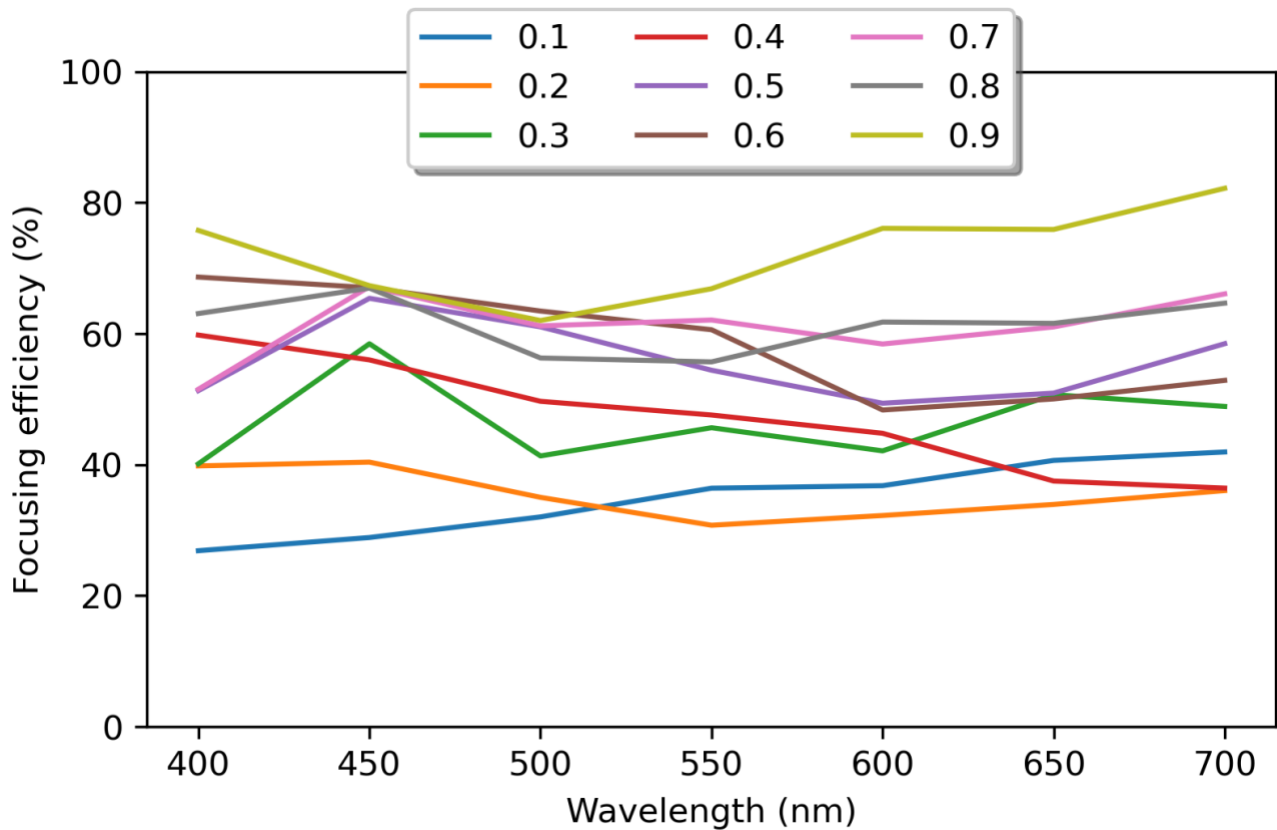


*Figure A: Focusing efficiency for each wavelength (400nm – 700nm) for all 9 numerical apertures between 0.1 and 0.9.*

### B. Computational Complexity

Our code is primarily run using Kaggle, a data science platform ubiquitously used by computational practitioners. Our notebooks are run on Kaggle’s kernels, which are free GPU-integrable Jupyter notebook servers, using dual-core Intel® Xeon® CPUs with 2.20 GHz refresh rate, with 32 GB of random access memory. The respective execution times for our metalens optimisation are reflected in terms of hours in Fig. B below.

Optimisation time per metalens

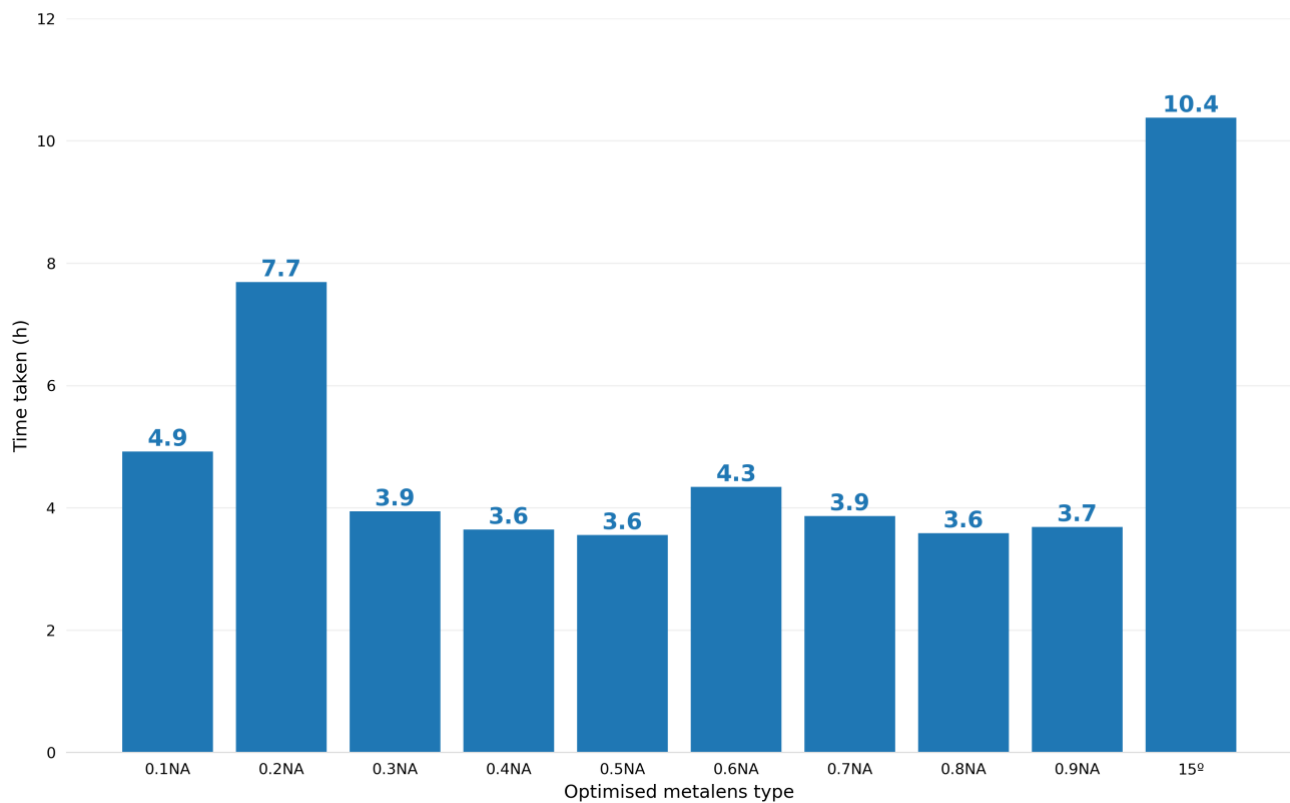


**Figure B:** The amount of execution hours taken to optimise each type of metalens design.

The average number of hours taken to optimise the achromatic and non-oblique metalenses is approximately 4.36 hours. It is important to note that execution times could be accelerated by exploiting parallelism — MEEP enables its users to divide their simulations into multiple processes, before running them in parallel on multi-core machines. Communication between different process is done using the Message Passing Interface (MPI) library, thus enabling dramatic speed-ups in certain cases. Even without the employment of simulation parallelism (as was true in our research), optimisation durations are still modest and manageable, not requiring heavy computational power nor an extensive amount of time in order to produce optimised designs for achromatic metalenses.